Article

An Observer-Based Current Sensor-Less Control Scheme for Grid-Following Converters

Mohamad Amin Ghasemi [1,*], Seyed Fariborz Zarei [2], Zahra Sohrabi [1], Frede Blaabjerg [3,*] and Saeed Peyghami [3]

1   Department of Electrical Engineering, Bu-Ali Sina University, Hamedan 6516738695, Iran; z.sohrabi@basu.ac.ir
2   Department of Electrical and Computer Engineering, Qom University of Technology, Qom 1519-37195, Iran; zarei@qut.ac.ir
3   Department of AAU Energy, Aalborg University, 9220 Aalborg, Denmark; sap@energy.aau.dk
*   Correspondence: ma.ghasemi@basu.ac.ir (M.A.G.); fbl@energy.aau.dk (F.B.)

Abstract: Distributed energy resources based on grid-following inverters are the dominant part of future modern power systems. To achieve a higher performance, the reliability enhancements and cost reductions of such inverters are the most important demands. In this respect, the sensors are one of the elements which greatly determine the cost and reliability of the inverters, and minimizing the number of sensors may achieve both lower costs and higher reliability. In addition, sensor data are prone to cyber-attacks, and sensor-less control techniques would improve the cyber-physical tolerance capabilities of the system. This paper proposes a grid-side current sensor-less control technique for grid-following inverters. In the proposed scheme, an observer is suggested which estimates the grid-side currents by processing the measured DC-link voltage. The estimated grid-side currents are fed to the control loops of the inverter. To verify the effectiveness of the proposed scheme, the stability of the overall control structure is analyzed, including the nonlinear dynamics of the DC-link voltage in the various operating points, using eigen value analysis and time domain simulations. The results demonstrate that the proposed scheme preserves the proper stability margin and performance of the GF-VSC, even in the presence of uncertainty in output filter inductance.

Keywords: grid-following inverter; observer; output current sensor; DC-link voltage; reliability; stability

1. Introduction

Grid-following (GFL) inverters are the fundamental elements of inverter-based distributed energy resources in the future, modern power systems. Currently, GFL inverters are increasingly adopted as the power conversion interface for grid integration of renewable energy resources [1]. In this regard, different studies are being conducted on current, power, and the DC-link voltage control of GFL inverters, with the focus on grid synchronization, especially in weak grid conditions with/without phase locked loop (PLL) [2–7], the stability of the phase locked loop (PLL), faults right through the capability of th eGFL inverters and their operation under faulty and unbalanced grid conditions [8–11], reliability enhancement and cost minimization with a reduction in the number of the required sensors in the control loops [12–22].

The grid integration of a GFL inverter is mainly done through L- or LCL-type filters to limit the harmonic current injection. An L-type filter has a weak harmonic attenuation characteristic, compared to the LCL filters. However, control with an L-type filter is simple, which makes it the preferred option for the grid integration of the GFL inverters. Typically, in the control of the GFL inverters with an L-type filter, at least two AC voltages, two AC currents and one DC-link voltage sensors are required. On the other hand, an LCL filter has superior attenuation characteristics compared to L-type filters, but at the cost of a complex

control structure to damp its resonance characteristics. To add more damping to the system, further sensors are required in the control structure.

In the case of sensor failures, the inverter usually loses its stability. Thus, proposing a control structure with a reduced number of the sensors is a key solution in improving the reliability of GFL inverters. In addition, the need to use a reduced number of sensors considerably decreases the cost and the complexity of the system. In this regard, different studies in the literature have tried to propose a control structure with a minimum number of the required sensors [12–22]. Specifically, active damping and control of the GFL inverters with an LCL filter requires the use of multiple signals, which necessitates the use of a reduced number of sensors for the sake of cost and complexity reduction. In this respect, using state observer-based control schemes are presented in the existing studies in the literature [12–15]. While the studies in [12,13] use only grid-side current sensors and grid voltage, the presented methods in [14,15] also eliminated the necessity for a grid voltage sensor. The conventional synchronization schemes of GFLs mostly rely on the use of measured grid-voltages. To remove the grid-voltage measurement from the control structure, virtual-flux observer-based [19] and grid voltage observer-based [16–18] methods are presented. However, current sensors are usually more expensive and their accuracy has more impact on the system-control performance. Therefore, the elimination of the grid current sensors has considerable effect on the cost reduction, reliability enhancement and fault tolerant capability under sensor failure. An observer-based robust current sensor-less control scheme is presented in [20] for the inverter-based multi-terminal direct current transmission system, which eliminates the current control loops and current measurements. In addition, reference [21] proposed a new control scheme for a double-fed induction generator, which substitutes the stator-current regulators for the rotor-current regulators, and eliminates the necessity for rotor-current measurement. A current sensor-less control scheme is presented in [22], for the control of a permanent magnet synchronous motor. Despite the different available studies, the presented methods are not applicable for GFL inverters.

To the best of the authors' knowledge, measuring the output current of the inverter is required in all of the presented control schemes in the literature, and there is no grid-side current sensor-less control scheme for GFL inverters. To cover this gap, this paper proposes a new scheme that controls the GFL inverter without requiring any grid-side current measurement. In the proposed control scheme, only the grid-side and DC-link voltages are used in the control system. Considering the obtained dynamic interaction between the grid-side current and the DC-link voltage, the grid-side currents are estimated via an observer-based controller. Accordingly, the measured currents are used in the control loop of the system. The novelties and contributions of the paper are summarized as follows.

1. Proposing an observer for the estimation of the grid-side currents of a GFL-inverter considering the nonlinear dynamics of DCLV;
2. Including the nonlinear model of DC-link voltage dynamic and the filter inductance instantaneous power in the estimation process;
3. Providing the well-proved eigenvalue analysis to verify the overall stability of the GFL inverter control system with the proposed observer.

Using the proposed scheme reduces the overall cost of manufacturing the GFL inverter and enhances its reliability and fault-tolerant capability.

The different parts of the paper are organized in seven complementary sections. In Section 2, the modeling of a GFL inverter with emphasize on the DCLV dynamic is presented. Conventional control of GFL inverter is explained in Section 3. III. The proposed scheme for the estimation of the grid-side currents is described in Section 4. The overall state-space model of the GFL inverter, with both the conventional and the proposed control schemes, is obtained in Section 5, and the stability of the overall system is studied in possible operating points. Various case studies and time-domain simulations are presented in Section 6, to show the effectiveness of the proposed scheme under different scenarios and dynamic conditions. Finally, the paper is concluded in Section 7.

2. Modeling of Grid-Following Inverter with L-Type Filter

Figure 1 shows a three-phase diagram of a GFL inverter with an L-type filter which delivers the power from the primary source to the grid. The state-space dynamic equation of the system consists of the dynamics of the grid-side currents and DC-link voltage in the "*abc*" frame as follows:

$$L\frac{di_{abc}}{dt} = v_{t(abc)} - v_{g(abc)} \tag{1}$$

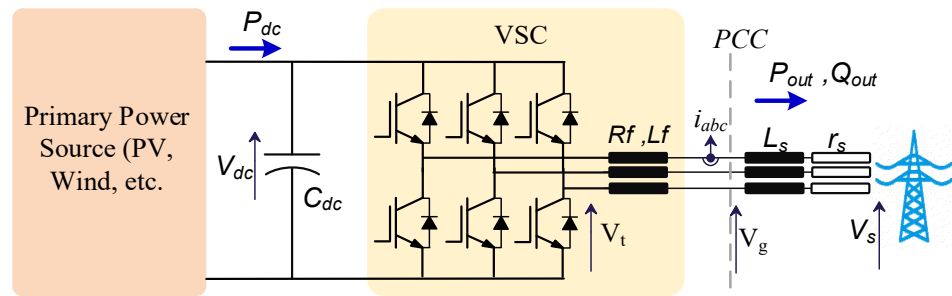$$\frac{d}{dt}\left(\frac{1}{2}C.v_{dc}^2\right) = P_{dc} - v_{t(abc)}i_{abc} \tag{2}$$

Figure 1. A GF-VSC.

In these equations and the associated Figure 1, L_f is the output filter, C_{dc} is the DC-link capacitor, v_{dc} is the DC-link voltage, P_{dc} is the power generated by the primary power source, $v_{t(abc)}$ is the VSC terminal voltage, $v_{g(abc)}$ is the grid (PCC) voltage, and $i_{(abc)}$ is the grid-side three phase currents. To remove the nonlinearity of (2), it is a common practice to use the DC-link energy $W_c = \frac{1}{2}C.v_{dc}^2$ instead of the DC-link voltage V_{dc} as a state variable. Using a phase-locked loop (PLL) based on $v_{g(abc)}$ and Park transformation, (1) and (2) can be shown by (3) in the "dq" frame representation form:

$$\begin{aligned}
\frac{di_d}{dt} &= -R_f i_d - w.i_q + \frac{(v_{td} - v_{gd})}{L_f} \\
\frac{di_q}{dt} &= -R_f i_q + w.i_d + \frac{(v_{tq} - v_{gq})}{L_f} \\
\frac{d}{dt}(W_c) &= P_{dc} - \frac{3}{2}\left(v_{td}i_d + v_{tq}i_q\right)
\end{aligned} \tag{3}$$

where i_q, i_d and v_{dc} are state variables; $v_{td} - v_{tq}$, and $v_{gd} - v_{gq}$ are the inverter and PCC voltages in the *d-q* frame, respectively. It can be seen that the DC-link voltage dynamic is still nonlinear, and (4) shows the dynamic equation, by substituting the grid-voltages instead of the terminal voltages:

$$\frac{d}{dt}(W_c) = P_{dc} - \frac{3}{2}\left(v_{gd}i_d + v_{gq}i_q\right) - P_{L-inst} \tag{4}$$

where P_{L-inst} is the instantaneous power of output filter, which is further expressed in (5):

$$P_{L-inst} = \frac{3}{4}L_f\frac{d}{dt}\left(i_d^2 + i_q^2\right) + \frac{3}{2}R_f\left(i_d^2 + i_q^2\right) \tag{5}$$

The first part models the change in the energy stored in the inductance of the filter and the second term models the conduction and switching losses in the inverter and output filter. To consider the worse possible condition from a stability perspective, the loss parts are ignored. Substituting (5) into (4) and with some simplification, the dynamic equation is as given in (6):

$$\frac{dW_c}{dt} = P_{dc} - \frac{3}{2}v_{gd}i_d - \frac{3}{2}L_f i_d\frac{di_d}{dt} - \frac{3}{2}L_f i_q\frac{di_q}{dt} \tag{6}$$

In addition, considering the zero value of v_{gq} in steady state due to the operation of PLL, the output active and reactive power of the inverter are as given in (7):

$$P_{out} = \tfrac{3}{2}v_{gd}i_d$$
$$Q_{out} = \tfrac{3}{2}v_{gd}i_q \tag{7}$$

It should be pointed out that the nonlinear terms in the right-hand side of (6) complicate the control design for this system. In order to alleviate the complexity of the nonlinear DC-link voltage dynamic, either a simplified model without non-linear parts or a linearized model with non-linear parts can be used.

The simplified model is as shown in (8):

$$\frac{d}{dt}W_c \approx P_{dc} - \frac{3}{2}v_{gd}i_d \tag{8}$$

Accordingly, the closed form of the state equations are as follows:

$$
\begin{bmatrix} \frac{di_d}{dt} \\ \frac{di_q}{dt} \\ \frac{dW_c}{dt} \end{bmatrix} = A_1 \begin{bmatrix} i_d \\ i_q \\ W_c \end{bmatrix} + B_{u-1} \begin{bmatrix} v_{td} \\ v_{tq} \end{bmatrix} + B_d \begin{bmatrix} v_{gd} \\ v_{gq} \\ P_{dc} \end{bmatrix}
$$
$$
y = C \begin{bmatrix} i_d \\ i_q \\ W_c \end{bmatrix} \text{ where,}
\tag{9}
$$

$$
A_1 = \begin{bmatrix} 0 & -\omega & 0 \\ \omega & 0 & 0 \\ -\frac{3}{2}v_{gd} & 0 & 0 \end{bmatrix} \quad B_{u-1} = \begin{bmatrix} 1/L_f & 0 \\ 0 & 1/L_f \\ 0 & 0 \end{bmatrix} \quad B_d = \begin{bmatrix} 1/L_f & 0 & 0 \\ 0 & 1/L_f & 0 \\ 0 & 0 & 1 \end{bmatrix} \quad C = [0\ 0\ 1] \tag{10}
$$

In the linearized model, the nonlinear terms are linearized at the operating point (P_{dc}, Q^{ref}) as follows:

$$\frac{d}{dt}W_c \approx P_{dc} - \frac{3}{2}v_{gd}i_d - \frac{3}{2}L_f\, i_d^{ss}\frac{di_d}{dt} - \frac{3}{2}L_f i_q^{ss}\frac{di_q}{dt} \tag{11}$$

According to (7) the operating point values of i_d and i_q are:

$$i_d^{ss} = P_{dc}/\left(\tfrac{3}{2}v_{gd}\right)$$
$$i_q^{ss} = Q^{ref}/\left(\tfrac{3}{2}v_{gd}\right) \tag{12}$$

Substituting (3) and (12) into (11) leads to the following linearized model of DC-link voltage dynamic:

$$\frac{d}{dt}W_c \approx P_{dc} - \frac{3}{2}v_{gd}i_d - \frac{3}{2}L_f i_d^{ss}\left(-\omega.i_q - \frac{R_f}{L_f}i_d + \frac{(v_{td}-v_{gd})}{L_f}\right) - \frac{3}{2}L_f i_q^{ss}\left(\omega.i_d - \frac{R_f}{L_f}i_q + \frac{(v_{tq}-v_{gq})}{L_f}\right) \tag{13}$$

By defining $a = -\frac{3}{2}L_f i_d^{ss}$, $b = -\frac{3}{2}L_f i_q^{ss} + \frac{3}{2}\frac{R_f}{w}i_d^{ss}$ and simplifying (13), the linearized model of DC-link voltage is represented by (13):

$$\frac{dW_c}{dt} = P_{dc} + \left(-\frac{3}{2}v_{gd} + bw\right)i_d - awi_q + a\frac{(v_{td}-v_{gd})}{L_f} + b\frac{(v_{tq}-v_{gq})}{L_f} \tag{14}$$

Despite the higher accuracy, the system model of (14) is dependent on the operating point, and is more complicated compared to (8). Based on (14), the closed form of the state-space equations is as follows:

$$
\begin{bmatrix} \frac{di_d}{dt} \\ \frac{di_q}{dt} \\ \frac{dW_c}{dt} \end{bmatrix} = A_2 \begin{bmatrix} i_d \\ i_q \\ W_c \end{bmatrix} + B_{u-2} \begin{bmatrix} \frac{1}{L_f} & 0 \\ 0 & \frac{1}{L_f} \\ \frac{a}{L_f} & \frac{b}{L_f} \end{bmatrix} \begin{bmatrix} v_{td} \\ v_{tq} \end{bmatrix} + B_{d-2} \begin{bmatrix} v_{gd} \\ v_{gq} \\ P_{dc} \end{bmatrix}
$$
$$
y = C \begin{bmatrix} i_d \\ i_q \\ W_c \end{bmatrix}
\tag{15}
$$

where,

$$
A_2 = \begin{bmatrix} 0 & -w & 0 \\ w & 0 & 0 \\ -\frac{3}{2}v_{gd}+bw & -aw & 0 \end{bmatrix} \quad B_{u-2} = \begin{bmatrix} 1/L_f & 0 \\ 0 & 1/L_f \\ 0 & 0 \end{bmatrix}
$$
$$
B_{d-2} = \begin{bmatrix} 1/L_f & 0 & 0 \\ 0 & 1/L_f & 0 \\ \frac{-a}{L_f} & \frac{-b}{L_f} & 1 \end{bmatrix} \quad C = [0\ 0\ 1]
\tag{16}
$$

It is worth mentioning that the model of (9) is the same as the model of (15), but in a special operating point, i.e., ($P_{dc} = 0$, $Q^{ref} = 0$).

3. Conventional Control of Grid-Following Inverters

The two main control purposes of a GFL-inverter are (i) delivery of the produced active power by the primary source to the grid and the exchange of the desired reactive power to the grid, according to the grid-codes, (ii) control of the DC-link voltage in the desired reference value. Both of the requirements should be met with a proper response time and stability margins.

According to (7), it is general practice to control the P_{out} and Q_{out} with i_d and i_q, respectively. In addition, according to (6), control of DC-link voltage at the predetermined value drives P_{out} to P_{dc}; and, accordingly, the desired P_{out} is delivered to the grid. Therefore, the control goals would be control of the reactive power and DC-link voltage, which are done via control of i_d and i_q. In this cascade control structure, the current control loops of i_d and i_q are inner loops, and the reactive power and DC-link voltage loops are outer control loops.

3.1. Current Control Loop

As shown by (3), there is a tight coupling between the i_d and i_q dynamics, and the grid voltages also affect the system dynamics. Hence, the proper decoupling actions and the feed-forward-based disturbance rejection approaches are required. Equation (15) provides the necessary control effort to cover both demands.

$$
\begin{aligned}
v_{td} &= L_f u_d + v_{gd} + R_f i_d + L_f w i_q \\
v_{tq} &= L_f u_q + v_{gq} + R_f i_q - L_f w i_d
\end{aligned}
\tag{17}
$$

where, u_d and u_q are intermediate control variables, which are introduced later on in (19). Substituting (17) into (3) yields to the resulted current dynamics of (16):

$$
\begin{aligned}
\frac{di_d}{dt} &= u_d \\
\frac{di_q}{dt} &= u_q
\end{aligned}
\tag{18}
$$

By defining the intermediate control variables of (17), the current control loop transfer functions are as given by (18), in which k_c is the current control loop bandwidth (BW):

$$\begin{cases} u_d = K_c \left(i_d^{ref} - i_d \right) \\ u_q = K_c \left(i_q^{ref} - i_q \right) \end{cases} \tag{19}$$

$$\begin{cases} i_d = \frac{K_c}{s+K_c} i_d^{ref} \\ i_q = \frac{K_c}{s+K_c} i_q^{ref} \end{cases} \tag{20}$$

K_c usually is chosen at least 10 times smaller than that of the switching frequency of VSC, to preserve the proper system stability in the presence of the time delay in the current control loop, imposed by computations and PWM switching in the control loop.

The current references of i_q^{ref} and i_d^{ref} are obtained from the reactive power and DC-link control loops, respectively.

3.2. Reactive Power Control Loop

The reactive power control loop determines i_q^{ref} using the reactive current setpoint of Q_{out} based on (21):

$$i_q^{ref} = \frac{Q^{ref}}{1.5v_{gd}} + \Delta i_q^{ref} \tag{21}$$

According to (7), using (21) and even without Δi_d^{ref}, Q_{out} is driven to Q^{ref}. However, uncertainty in the system, the delays in the current control loop, and the simplification in the system model may lead to a steady state error in controlling Q_{out}. To guarantee a zero steady-state error, a PI controller is also used, which provides the Δi_q^{ref} by (22):

$$\Delta i_d^{ref} = \frac{K_{p-q}s + K_{i-q}}{s} \left(Q^{ref} - Q_{out} \right) \tag{22}$$

The bandwidth of the reactive power control loop is chosen at least four times lower than that of the i_q control loop.

3.3. DC-Link Control Loop

Considering the three dynamic models for the DC-Link presented in Equations (3), (8) and (14), three schemes can be used for DC-link control [23], which are:

Using the simplified DC-Link model of (8) and designing a PI controller. This method is the prevalent control design scheme in the literature, known as "conventional DC-link control scheme";

Using the operating point-dependent model of (14) and designing an adaptive DC-link controller;

Using the nonlinear dynamic model of (3) and designing a nonlinear DC-link controller for a complicated system.

Among the above options, using the simplified DC-link model of (8) results in a simplified control design. However, it imposes restrictions on the bandwidth of the DC-link control loop, especially in rectifying mode. The deficiency of the restricted bandwidth, and accordingly the poor disturbance rejection capability, can be solved by using a larger DC-link capacitor. As a result, this method is a commonly used approach in the literature for finding the "d" axis current reference. According to (8), the DC-link voltage dynamic depends on both i_d and P_{dc}. To cancel the impact of P_{dc}, it is considered as a measurable disturbance and compensated for by feedforward control. Finally, i_d^{ref} is determined as given by (21):

$$i_d^{ref} = \frac{P_{dc}}{1.5v_{gd}} + \frac{K_{p-wc}s + K_{i-wc}}{s} \left(W_c^{ref} - W_c \right) \tag{23}$$

It is worth mentioning that the bandwidth of the DC-link control loop is selected at least four times lower that of i_d control loop. In addition, reducing the bandwidth improves the system stability, considering the uncertainty in the model of (8).

4. Proposed Observer and Control Structure

According to the control structure of the GFL-inverter, the grid-side currents, the grid voltages and the DC-link voltage are required for control of the inverter. By analyzing the system dynamic equation of (3), it can be seen that there is a coupling between W_c, i_d, and i_q. Then, theoretically, it is possible to estimate the grid currents (i_d, and i_q) by measuring the DC-link voltage. This is the key idea of this paper in developing an observer for the grid-side current estimation. In this respect, a well-adapted Luenberger observer is used in this paper, as the system is observable. In the following subsection, the fundamentals of the Luenberger observer are presented.

4.1. Fundamentals of the Luenberger Observer

Generally, the Luenberger observer is designed for linear systems with the given block diagram of Figure 2. This figure consists of three main blocks of (i) the real system, (ii) a dynamic model of the system, and (iii) Matrix L. The goal of the observer is the accurate estimation of the state variables of the system. The best dynamic response and accurate estimation is achieved if the dynamic model of the system accurately models the real system. In other words, it is proved that by providing the accurate state-space dynamic equation of the system, the correct initial conditions, and the inputs of the real system into the simulated state-space equation, the response of the simulated system, including the output and state variables, are equal to those of the real system.
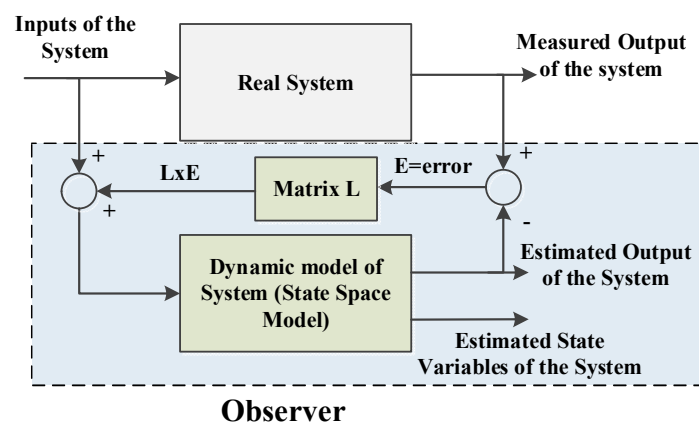

Figure 2. State-space variable observer and its operation mechanism beside the real system.

However, the model of the system may have some uncertainties. In addition, the initial values of the state variables in the real system are not available, and using them in the simulated system is not feasible. To compensate for this deficiency, the error between the measurable output of the real system and that of the simulated system is calculated and multiplied with a matrix, i.e., observer matrix L. The results are fed back to the simulated system, which finally reduces the error values. In an observable system, it is proved that all of the errors between the state variables of the real system and the simulated system are driven to zero by choosing a proper value for matrix L. Accordingly, the time-domain waveforms of the state variables of the simulated system become equal to those of the real system. By this procedure, the state variables of the real systems are obtained without using a direct measurement tool. The details of the Luenberger observer design procedure can be found in [24], which is not further elaborated for the sake of brevity. The application of the Luenberger observer for the control of the GFL-inverter is provided in the following subsection.

4.2. Estimation of the Grid-Side Currents Using Luenberger Observer

In this subsection, the presented Luneburg observer is applied on a GFL inverter to estimate the grid-side currents. As mentioned before, this observer is appliable on linear system, and the linearized equations of the system are required for the design procedure. In this regard, considering the nonlinear dynamics of the DC-link control, the models of either (8) or (13) can be used in the observer-design procedure. In the grid current estimation, there are two alternatives of:

1. Using the system model in (9) for the observer design, which includes the simplified linear DC-link model of (8);
2. Using the system model in (15) for the observer design, which includes the linearized operating point-dependent DC-link model of (13).

As a rule of thumb, it is clear that using (9) leads to a simple design process; however, the approximation of (9) may lead to an undesirable response. On other side, (15) is an operating point-dependent model, and consequently, an adaptive observer, such as a gain-scheduling observer, should be designed. To make a compromise, the observer is designed for the middle operating point of $P_{mid} = \left(P_{dc} = P_{nom}/2, Q^{ref} = 0 \right)$ in this paper, which still can be used for all of the operating points. Therefore, it imposes less approximation compared to (9) on average. Based on the Luenberger observer design scheme, the state-space equation of the observer consists of (1) state-space equation of the main system and (2) a compensating term. Considering the GFL-inverter linearized model of (15) in the middle operating point P_{mid}, the observer state-space equations can be written as (24):

$$\frac{\widehat{dX(t)}}{dt} = A_2|_{P_{mid}} \widehat{X(t)} + B_{u2}|_{P_{mid}} \begin{bmatrix} v_{td} \\ v_{tq} \end{bmatrix} + B_d|_{P_{mid}} \begin{bmatrix} v_{gd} \\ v_{gq} \\ P_{dc} \end{bmatrix} + L_{3X1} \left(CX(t) - C\widehat{X(t)} \right) \quad (24)$$

In this equation, the last term is the compensating term; other terms are a model of the system at P_{mid}, the matrix $L = [L_1\ L_2\ L_3]^T$ is the observer matrix with three elements, $X(t) = [i_d\ i_q\ W_c]$ is the estate vector, and $\widehat{X(t)} = \left[\hat{i}_d,\ \hat{i}_q,\ \widehat{W_C} \right]$ is the estimated state vector. In $\widehat{X(t)}$, $\hat{i}_d$ and $\hat{i}_q$, are, respectively, the estimated values of the grid current in d and q axes, and $\widehat{W_c}$ is the estimated value of the DC-link energy. As the DC-link energy is directly measured, its estimation is not used in the control structure. Inputs of the observer are W_c, v_{gd}, v_{gq}, P_{dc} (if available), and the control variables of v_d and v_q. Based on the Luenberger observer design scheme, the observer matrix L must be determined in such a way that all of the eigenvalues of the matrix $\left(A_2|_{P_{mid}} - LC \right)$ become stable.

It is worth noting that the first proposed observer in (24) is a third-order system. Considering the order of the system, which is three, and the measured value of W_c, it is possible to estimate the i_d and i_q by a second-order observer (reduced order observer). This may lead to a lower computational burden in the control loop. However, to include the nonlinear DC-link model in the observer implementation, it is necessary to use the third-order observer, which considerably increases the performance. Moreover, although matrix L and the compensating term of the observer are designed based on a linearized model of (24), the exact nonlinear model of the system can be used in the final form of the observer. Accordingly, the observer of (24) is replaced by (25), which includes the nonlinear DC-link dynamics of the system:

$$\begin{aligned} \frac{d\hat{i}_d}{dt} &= -w.\hat{i}_q + \frac{(v_{td} - v_{gd})}{L_f} + L_1 \left(W_c - \widehat{W_c} \right) \\ \frac{d\hat{i}_q}{dt} &= w.\hat{i}_d + \frac{(v_{tq} - v_{gq})}{L_f} + L_2 \left(W_c - \widehat{W_c} \right) \\ \frac{d}{dt} \left(\widehat{W_c} \right) &= P_{dc} - \frac{3}{2} \left(v_{td}\hat{i}_d + v_{tq}\hat{i}_q \right) + L_3 \left(W_c - \widehat{W_c} \right) \end{aligned} \quad (25)$$

In summary, first, a constant observer matrix L is designed, based on the system model of (15) in middle operating point P_{mid}, and then it is used in the compensating term beside the exact nonlinear model of the system to complete the observer dynamic, as in (25).

Figure 3 shows the block diagram of the overall system, including the controller, observer and the GFL-inverter power circuit. It can be seen that only the grid voltages and the DC-link voltage are measured, and using the proposed scheme, the estimated values of the grid currents ($\widehat{i_{td}}$, $\widehat{i_{tq}}$) are used as feedback signals in the control loop, instead of measuring (i_{td}, i_{tq}). In this structure, the three current sensors of the GFL-inverter are eliminated, and the terminal voltages description of the inverter will be as shown by (26):

$$v_d = L_f K_c \left(i_d^{ref} - \widehat{i_d} \right) + v_{gd} + R_f \widehat{i_d} + L_f w \widehat{i_q}$$
$$v_q = L_f K_c \left(i_q^{ref} - \widehat{i_q} \right) + v_{gq} + R_f \widehat{i_q} - L_f w \widehat{i_d}$$
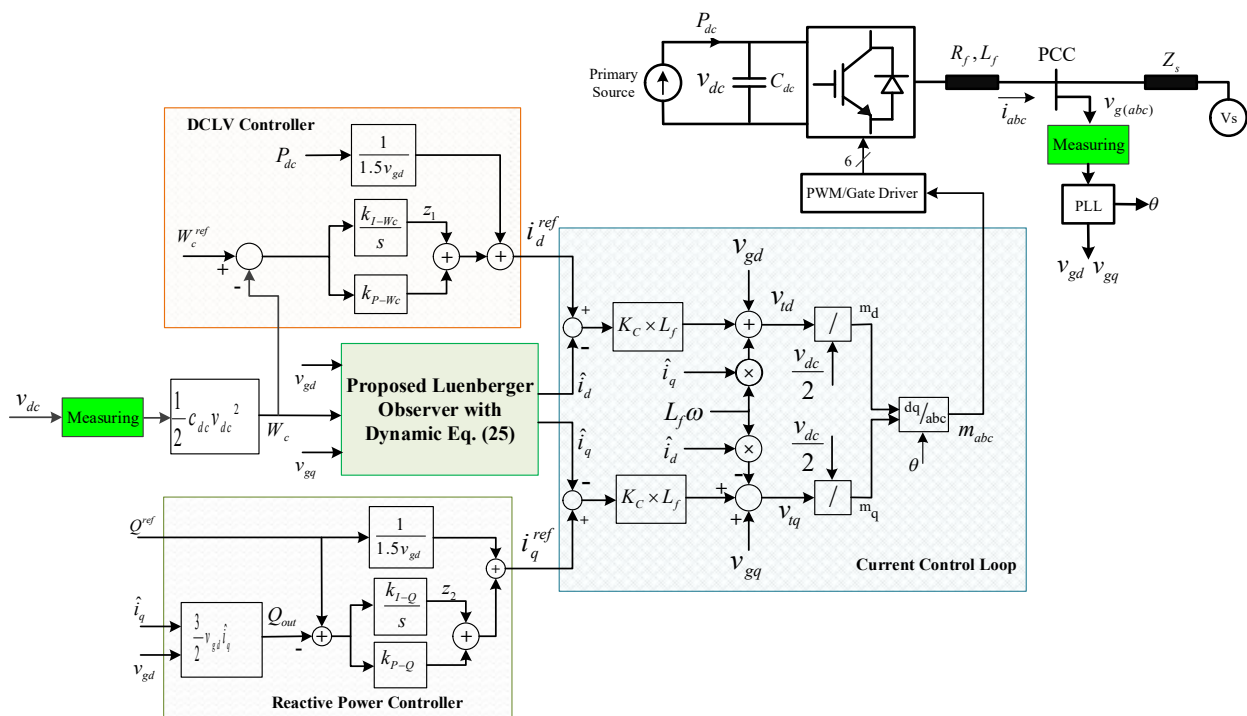
(26)

Figure 3. Complete control block diagram of a GFL-inverter including (i) the proposed observer control scheme; (ii) DCLV controller; (iii) reactive power controller; (iv) current control loop; (v) measured DC-link voltage and grid-side voltages.

5. Stability Analysis of the GF-VSC with the Proposed Observer

The stable operation with a high-enough stability margin is the preliminary requirement of a given control system. In this section, the stability of the GFL-inverter with the proposed observer and control structure is analyzed, using the eigenvalue theory. To cover all of the dynamics of the system, the dynamic model of the grid-side current and the DC-link voltage of (14), the observer dynamic of (25), and the controllers of (21) and (23) are integrated and used to obtain the overall system model. It should be mentioned that, for stability analysis by eigen values, a linearized model of the overall system is needed. A linearized state-space model of the primary system was presented in (15), also, the linearized model of the observer in (25) is given by (27):

$$\frac{\widehat{dX(t)}}{dt} = A_2 \widehat{X(t)} + B_{u2} \begin{bmatrix} v_{td} \\ v_{tq} \end{bmatrix} + B_d \begin{bmatrix} v_{gd} \\ v_{gq} \\ P_{dc} \end{bmatrix} + L \left(CX(t) - C\widehat{X(t)} \right)$$

(27)

Therefore, it is only needed to extract the state-space model of controllers, to complete the state-space model of the overall system shown in Figure 3. According to the block diagram in Figure 3, the two state variables of z_1, z_2 are defined to represent the controller in the state-space equations as follows:

$$\frac{dz_1}{dt} = k_{I-Wc}\left(W_c^{ref} - W_c\right)$$
$$\frac{dz_2}{dt} = k_{I-Q}\left(Q^{ref} - Q\right) = k_{I-Q}\left(Q^{ref} - 1.5v_{gd}\widehat{i_q}\right) \tag{28}$$

Furthermore, based on the block diagram of the system in Figure 3, the control variables of v_{td} and v_{tq} are as given in (29):

$$v_{td} = v_{gd} + L_f w\widehat{i_q} + R_f\widehat{i_d} + L_f k_C\left(i_d^{ref} - \widehat{i_d}\right)$$
$$v_{tq} = v_{gq} - L_f w\widehat{i_d} + R_f\widehat{i_q} + L_f k_C\left(i_q^{ref} - \widehat{i_q}\right) \tag{29}$$

In which, the current references of i_d^{ref} and i_q^{ref} are given in (30):

$$i_d^{ref} = \frac{P_{dc}}{1.5v_{gd}} + z_1 + k_{P-Wc}\left(W_c^{ref} - W_c\right)$$
$$i_q^{ref} = \frac{Q^{ref}}{1.5v_{gd}} + z_2 + k_{P-Q}\left(Q^{ref} - 1.5v_{gd}\widehat{i_q}\right) \tag{30}$$

Substituting (30) into (29), and with some simplification, the result is as given in (31):

$$\begin{bmatrix} v_{td} \\ v_{tq} \end{bmatrix} = \begin{bmatrix} v_{gd} \\ v_{gq} \end{bmatrix} + B_{new-x}X + B_{new-\widehat{x}}\widehat{X} + B_{new-z}Z \tag{31}$$

where,

$$B_{new-x} = \begin{bmatrix} 0 & 0 & -L_f K_C K_{P-Wc} \\ 0 & 0 & 0 \end{bmatrix}$$
$$B_{new-\widehat{x}} = \begin{bmatrix} -L_f K_C & L_f w & 0 \\ -L_f w & L_f K_C\left(-1 - 1.5v_{gd}K_{P-Q}\right) & 0 \end{bmatrix} \tag{32}$$
$$B_{new-z} = \begin{bmatrix} L_f K_c & 0 \\ 0 & L_f K_c \end{bmatrix}$$

It is worth noting that the inputs of the system W_c^{ref}, Q^{ref} and P_{dc} do not affect the stability of the system, and they are eliminated in (31) for the stability analysis. Applying the control variables of (31) into the linearized model of the system and observer in (15) and (27), then by merging with the controller-state equations of (28), the resultant linearized model of the overall system is given in (33):

$$\frac{dX(t)}{dt} = A_2 X(t) + B_{u2}B_{new-X}X(t) + B_{u2}B_{new-\widehat{X}}\widehat{X}(t) + B_{u2}B_{new-z}Z(t)$$
$$\frac{d\widehat{X(t)}}{dt} = A_2\widehat{X(t)} + B_{u2}B_{new-X}X(t) + B_{u2}B_{new-\widehat{X}}\widehat{X}(t) + B_{u2}B_{new-z}Z(t)$$
$$+ L\,C\left(X(t) - \widehat{X}(t)\right) \tag{33}$$
$$\frac{dZ(t)}{dt} = \left(K_X = \begin{bmatrix} 0 & 0 & -k_{I-Wc} \\ 0 & 0 & 0 \end{bmatrix}\right)X(t) + \left(K_{\widehat{X}} = \begin{bmatrix} 0 & 0 & 0 \\ 0 & -1.5v_{gd}k_{I-Q} & 0 \end{bmatrix}\right)\widehat{X}(t)$$

The closed form of (31) is written in (34):

$$\frac{d}{dt}\begin{bmatrix} X(t) \\ Z(t) \\ \widehat{X(t)} \end{bmatrix} = \begin{bmatrix} A_2 + B_{u2}B_{new-X} & B_{u2}B_{new-z} & B_{u2}B_{new-\widehat{X}} \\ K_X & 0 & K_{\widehat{X}} \\ LC + B_{u2}B_{new-X} & B_{u2}B_{new-z} & A_2 + B_{u2}B_{new-\widehat{X}} - LC \end{bmatrix}\begin{bmatrix} X(t) \\ Z(t) \\ \widehat{X(t)} \end{bmatrix} \tag{34}$$

The stability of the overall control system is dependent on the eigenvalues of the state matrix of (34). Given that A_2 and B_{u2} are dependent on the operating points of GFL inverter

(P_{dc}, Q^{ref}), the eigenvalues of the state matrix of (34) should be analyzed in a full range of operating points. In addition, the eigenvalues of the conventional control system without an observer are presented for comparison purposes.

In the case study and numerical analysis, a sample GFL-inverter, with the characteristic parameters given in Table 1, is used in the following.

Table 1. Parameter Values of the studied system.

Parameters	Values
Nominal Power of VSC	10 kW
Grid Frequency	50 Hz
L_f	8.6 mH
DC-link Capacitor	200 uF
Grid impedance (Z_s)	$0.1 + j1$
Grid Voltage	380 V
K_{P-Wc}	$232/v_{gd}$
K_{I-Wc}	$67/v_{gd}$
K_{P-Q}	0
K_{I-Q}	$33/v_{gd}$
K_c	2000
Observer Matrix L	$1 \times 10^4 \, [-3.08 \; 6.76 \; 0.065]^T$

Figure 4 shows the poles of the GFL inverter with a conventional control system without using an observer in different operating points. From the figure, it can be seen that the system is a fifth-order system, and increasing the P_{dc} would shift the poles to the more negative values. In addition, Q^{ref} does not affect the poles, and hence, the poles are shown only for $Q^{ref} = 0$. Furthermore, all of the poles have a damping coefficient of $\zeta = 1$ regardless of the operating points.
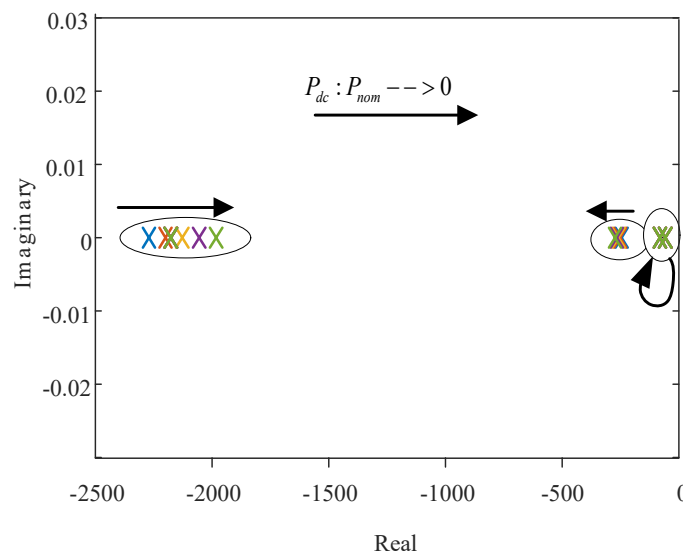

Figure 4. The poles of the overall control system with conventional controller in different operating points without observer.

In the design of matrix L, it is possible to place the observer poles of $OBS_{Poles} = Eigen(A_2|_{P_{mid}} - LC) = [P_1 \; P_2 \; P_3]$ at any of the desired values. The negative poles with higher values provide a higher bandwidth and increased observer speed, which consequently decreases the estimation error in the presence of uncertainty in the model of the system. However, it may deteriorate the stability of the closed loop system in the presence of uncertainty. To further evaluate the effect of the observer poles on the stability of the overall system in various operating points, $\left(P_{dc}, Q^{ref}\right)$ are illustrated in Figure 5.

Four cases for the poles of the observer are examined. Suppose that the four-observer matrix is designed in such a way that the poles of the observer are as follows.

$$
\begin{aligned}
\text{Observer 1}: \ OBS_{Poles} &= -2.5[1.1K_c \ 1K_c \ 0.9K_c] \\
\text{Observer 2}: \ OBS_{Poles} &= -1.7[1.1K_c \ 1K_c \ 0.9K_c] \\
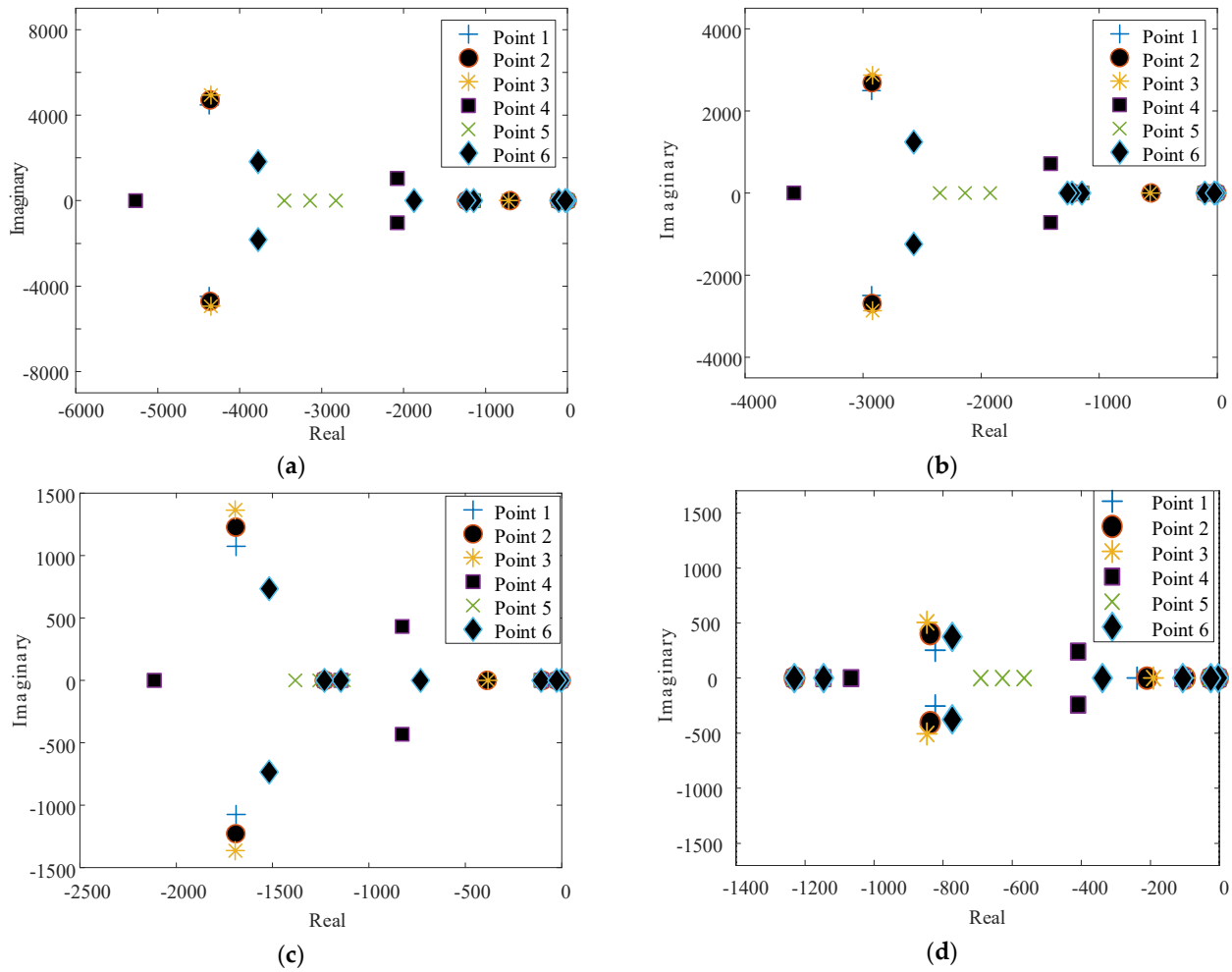\text{Observer 3}: \ OBS_{Poles} &= -1[1.1K_c \ 1K_c \ 0.9K_c] \\
\text{Observer 4}: \ OBS_{Poles} &= -0.5[1.1K_c \ 1K_c \ 0.9K_c]
\end{aligned}
\tag{35}
$$

Figure 5. The change of the overall system poles for 4 different observers in 6 different operating points, (**a**) Observer 1; (**b**) Observer 2; (**c**) Observer 3; (**d**) Observer 4.

In this study, the position of the poles ($[P_1, P_2, P_3]$) are chosen depending on the current control-loop bandwidth (K_c), and P_1, P_2, and P_3 are considered similar to each other. Figure 5 shows the eigenvalues of the closed loop system for the four observers of Observer#1-to- Observer#4 in the six operating points under the full range of active power and reactive power production, as given in (36):

$$
\begin{aligned}
\left(P_{dc}, Q_{ref} \right) &= \{ \{ Point\ 1, Point\ 2, Point\ 3, Point\ 4, Point\ 5, Point\ 6 \} \\
&= \{ (P_{nom}, -0.4P_{nom}), (P_{nom}, 0), (P_{nom}, 0.4P_{nom}), (0, -0.4P_{nom}), (0, 0), (0, 0.4P_{nom}) \}
\end{aligned}
\tag{36}
$$

From Figure 5, it can be seen that the overall system is stable for all four observers in all six operating points. In addition, increasing the observer bandwidth moves the poles to the far away points in the s-plane, but as expected, decreases the poles damping coefficient ζ. This is due to the difference between the model of (24), used for the design

of matrix *L*, and the exact model of system in (3). Moreover, it decreases the delay margin of the system, which, considering the time delay imposed in the control loop by VSI, may destabilize the system. On the other hand, reducing the observer bandwidth may increase the estimation error in the presence of the uncertainty. Accordingly, a compromise is needed in the selection of the observer bandwidth and the system stability. In this regard, the third observer, whose corresponding matrix *L* is presented in Table 1, is chosen as the final observer.

6. Case Studies, Numerical Results, and Discussions

The performance of the proposed observer and controller is evaluated through the various case studies on the sample test system in this section. The complete characteristics of the system are presented in Table 1.

To evaluate the performance of the system under different operating conditions, different values and changes are applied to P_{dc}, Q^{ref}, and W_c^{ref}. Both the actual and estimated grid-side currents, the DC-link voltage, and the active and reactive powers are presented. In addition, the system performance in the presence of uncertainty in the output filter inductance is examined. The detail of the scenarios is as follows.

Initially, the values are set at $P_{dc} = 10$ kW, $Q^{ref} = 0$ kVAR, and $V_{dc}^{ref} = 750$ V. A step-up and a step-down command are given to Q^{ref}, respectively. Then, a step-up and a step-down command are applied to V_{dc}^{ref}, respectively. Furthermore, P_{dc} is gradually changed from 10 kW to 0 kW. While P_{dc} is 0 kW, another step-up and a step-down command is given to Q^{ref} and V_{dc}^{ref}. The changes in the reference values (P_{dc}, Q^{ref}, and W_c^{ref}) are shown in Figure 6. To make the simulation tests close to the practical experimental tests, zero order hold sampling, PWM and a computation delay of $T_d = 1/(2f_s)$ are also intended in the simulations. The simulation results are presented in Figures 6 and 7.
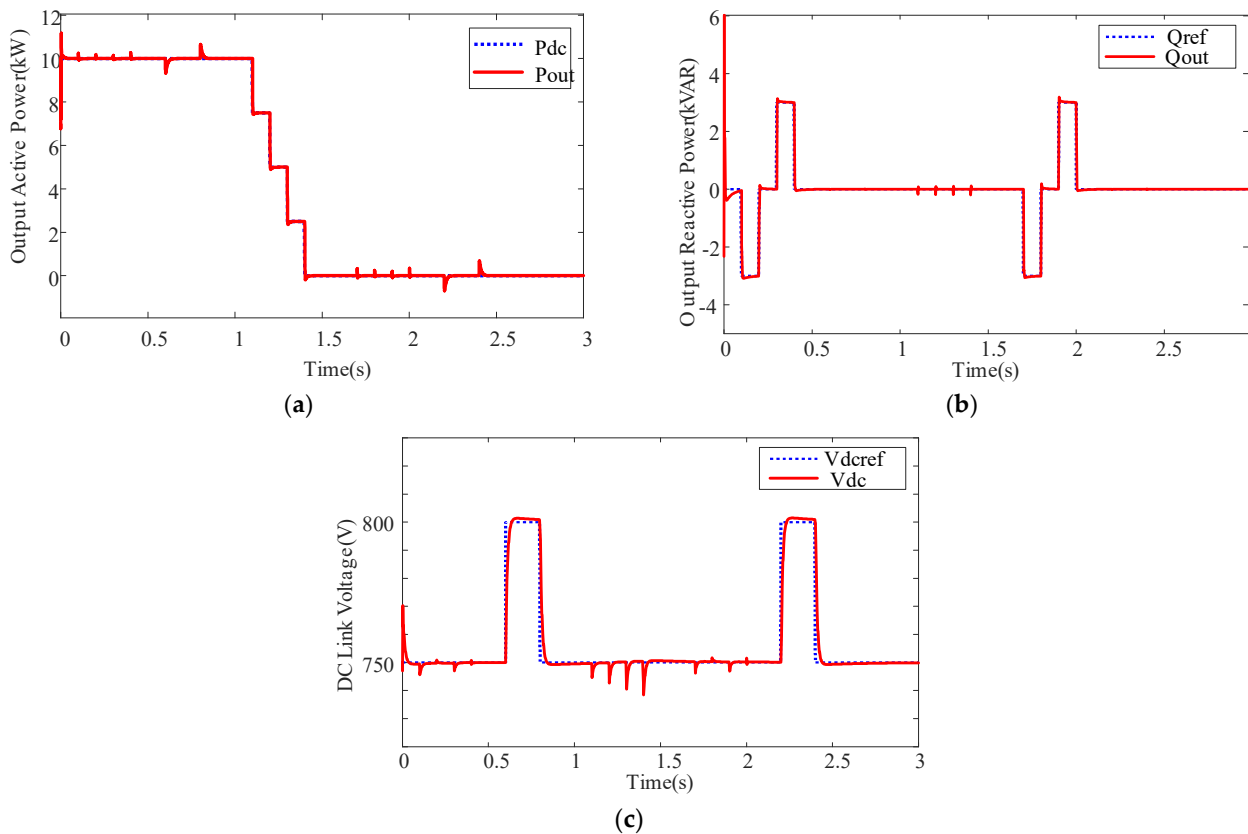

Figure 6. Dynamic response of the overall system consists of (**a**) P_{out}; (**b**) Q_{out}; and (**c**) V_{dc} with their reference values when the observer is used in the control loop of GFL inverter.
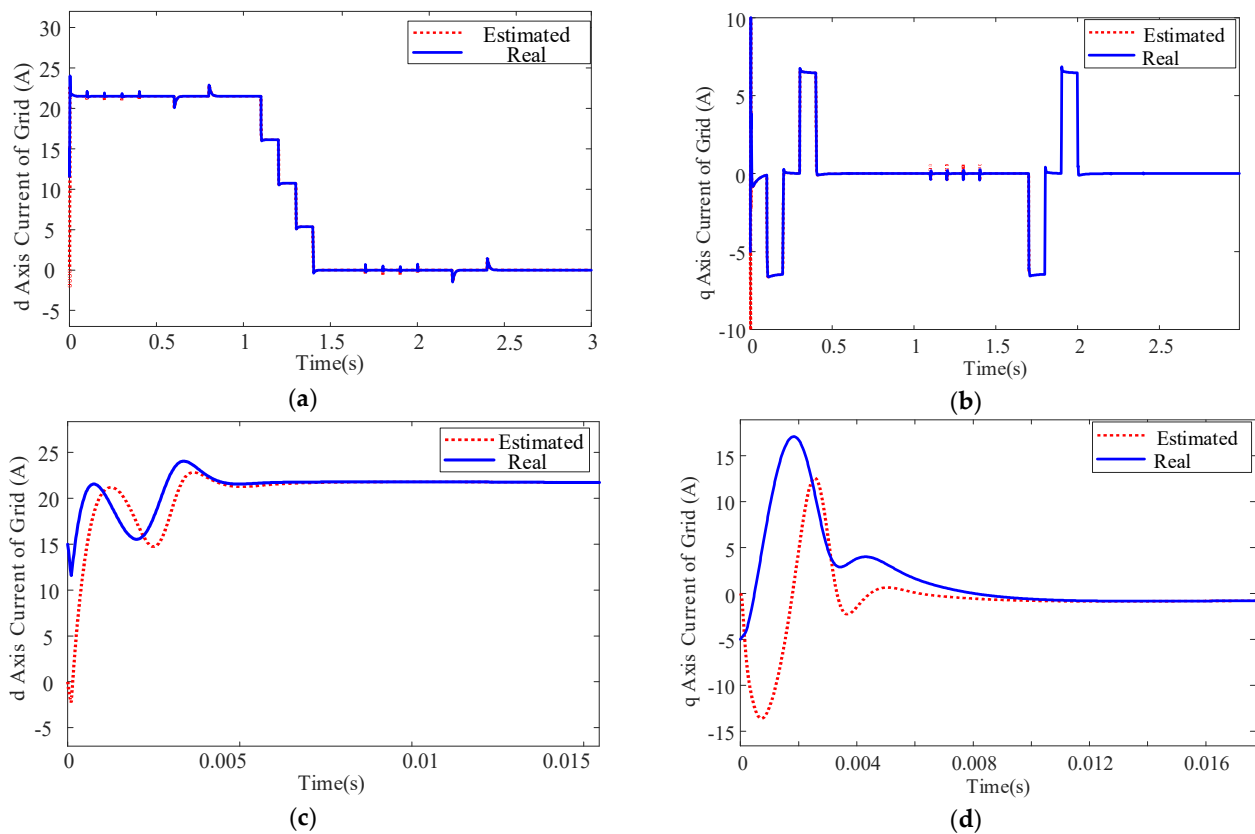
Figure 7. *D* and *q* Axis value of grid currents (real and estimated value): (**a**) *d* axis current; (**b**) *q* axis current; (**c**) zoomed view of *d* axis current in startup; and (**d**) zoomed view of *q* axis current in startup.

Figure 6 shows that using the proposed control scheme, including the proposed observer, DC-link voltage and Q_{out} of the GFL inverter, properly tracks their reference values with a fast dynamic response and a high stability margin. In other words, Figure 7 shows that using the observer in the control loop of the GFL inverter instead of the grid-side current measurement, does not affect the dynamic performance of the overall GFL inverter. Also, as shown in Figure 7, the estimated currents $\hat{i}_d$ and $\hat{i}_q$ are driven to their actual values very fast in startup and under the reference values variation. In addition, for better vision, the zoomed view of deriving $\hat{i}_d$ and $\hat{i}_q$ to their actual values in the startup time are shown in Figure 6c,d, which demonstrates the proper performance of the proposed observer.

Moreover, to show the robustness under the presence of uncertainties, a 20% uncertainty in the output filter is considered. It is supposed that the actual L_f is 20% larger than the value used in the design of the observer and the control loop. In addition, as another scenario, it is supposed that the actual L_f is 20% smaller than the value used in the design of the observer and the control loop. The simulation results in Figure 8 show that such large uncertainties in the L_f value partially affect the system performance. It negligibly decreases the speed of the system in tracking the reference values of reactive power and DC-link voltage. Such minor effects can be ignored, since the important features of the system, including the tracking capability, dynamic performance, high functionality and stability margin of the system, are preserved even under the presence of the uncertainty in the model of the system.

The different case studies and scenarios and the obtained results demonstrate that the proposed control scheme effectively provides proper performance even with a reduced number of measurement signals. This provides the manufacturers of the GFL inverter with an opportunity to reduce the cost and increase the reliability of the inverters by reducing the number of required sensors.
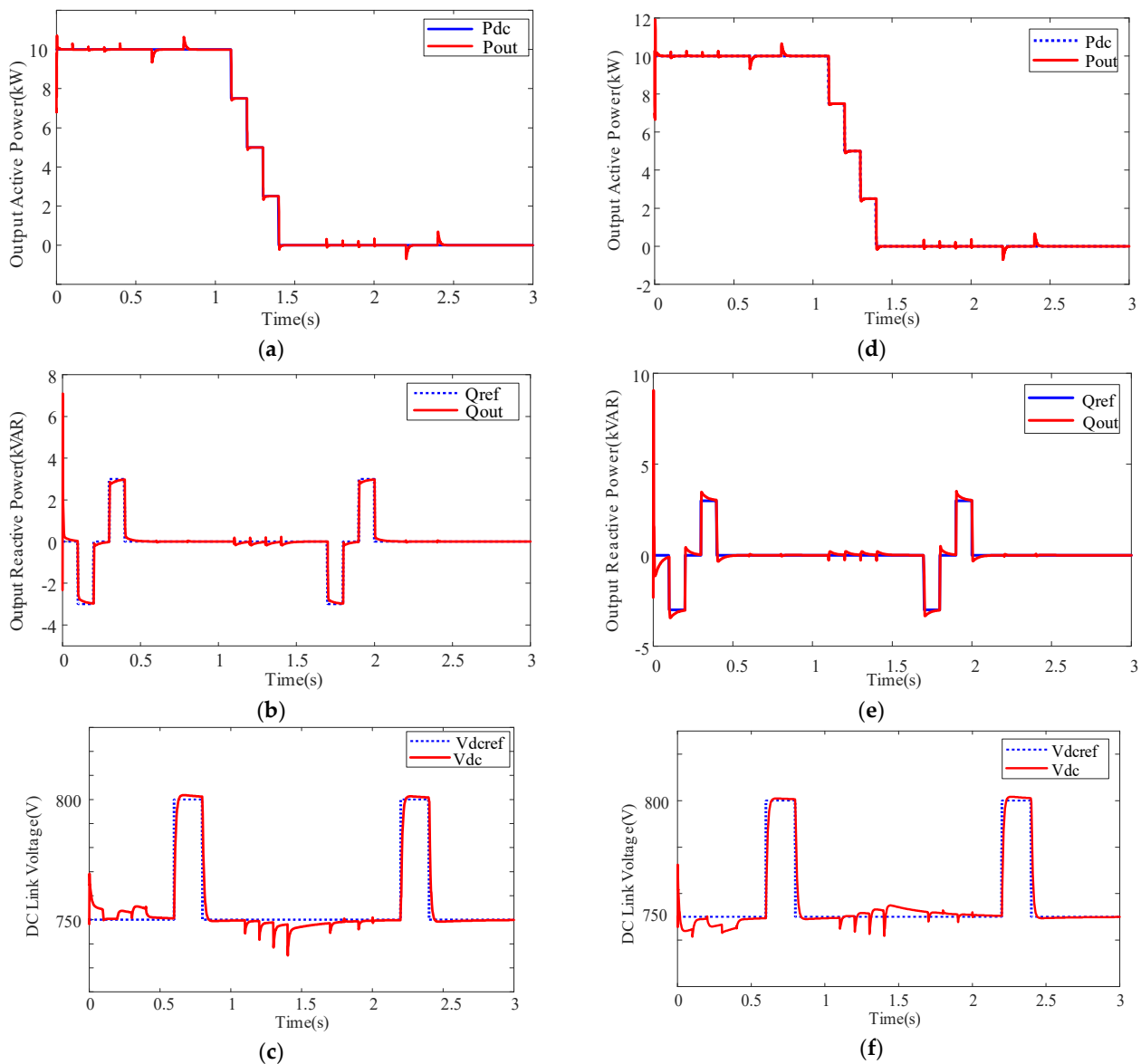
Figure 8. Dynamic response of the system in the presence of uncertainty in output filter inductance, (**a**–**c**) output active and reactive power and DC-link voltage of the GFL inverter in presence of +20% uncertainty in L_f, and (**d**–**f**) output active and reactive power and DC-link voltage of the GFL inverter in presence of −20% change in L_f.

7. Conclusions

In this paper, the control of a GF-inverter with an L-type filter is studied and the idea of estimating the output filter current was proposed. In the proposed idea, the output filter currents were estimated with an observer-based controller, which eliminates the need to use the grid-side current sensors. Using a lower number of sensors, the total cost of the system is reduced, and the reliability and fault-tolerant capability of the GF inverter are increased. To develop the analytical formulation of the proposed idea, modeling of the GF inverter with a focus on the DC-link voltage dynamic model is presented. It is shown that the output filter currents are observable and can be estimated by measuring the DC-link voltage and employing a linear observer. In the design of the observer matrix, the linearized model of the non-linear DC-link voltage dynamic is used, which provides a simple constant observer with proper accuracy. To increase the performance in estimating the real system dynamics, the nonlinear model of DC-link voltage is employed in the observer implementation. Moreover, the stability of overall system is evaluated by using

the system state-space equations in different operating points through eigenvalue analysis. Various time domain simulation in MATLAB/SIMULINK and case studies verify the proper suitable tracking, estimation functionality, dynamic performance, and stability margin of the proposed control system in all operating pints even under presence of uncertainty in output filter inductance.

References

1. Zarei, S.F.; Mokhtari, H.; Ghasemi, M.A. Enhanced control of grid forming VSCs in a micro-grid system under unbalanced conditions. In Proceedings of the 2018 9th Annual Power Electronics, Drives Systems and Technologies Conference (PEDSTC), Tehran, Iran, 13–15 February 2018; pp. 380–385.
2. Zarei, S.F.; Ghasemi, M.A.; Peyghami, S.; Davari, P.; Mokhtari, H.; Blaabjerg, F. Characterization of Proportional-Integral-Resonant Compensator for DC Link Voltage Control. In Proceedings of the 2018 IEEE 19th Workshop on Control and Modeling for Power Electronics (COMPEL), Padua, Italy, 25–28 June 2018; pp. 1–8.
3. Mansour, M.Z.; Ravanji, M.H.; Karimi, A.; Bahrani, B. Small-Signal Synchronization Stability Enhancement of Grid-Following Inverters via a Feedback Linearization Controller. *IEEE Trans. Power Deliv.* **2022**, 1. [CrossRef]
4. Hu, P.; Chen, Z.; Yu, Y.; Jiang, D. On Transient Instability Mechanism of PLL-Based VSC Connected to a Weak Grid. *IEEE Trans. Ind. Electron.* **2022**, 1–11. [CrossRef]
5. Bahrani, B. Power-Synchronized Grid-Following Inverter Without a Phase-Locked Loop. *IEEE Access* **2021**, *9*, 112163–112176. [CrossRef]
6. Saenz-Aguirre, A.; Zulueta, E.; Fernandez-Gamiz, U.; Teso-Fz-Betoño, D.; Olarte, J. Kharitonov theorem based robust stability analysis of a wind turbine pitch control system. *Mathematics* **2020**, *8*, 964. [CrossRef]
7. Zarei, S.F.; Mokhtari, H.; Ghasemi, M.A.; Peyghami, S.; Davari, P.; Blaabjerg, F. DC-link loop bandwidth selection strategy for grid-connected inverters considering power quality requirements. *Int. J. Electr. Power Energy Syst.* **2020**, *119*, 105879. [CrossRef]
8. Wu, H.; Wang, X. Design-Oriented Transient Stability Analysis of PLL-Synchronized Voltage-Source Converters. *IEEE Trans. Power Electron.* **2020**, *35*, 3573–3589. [CrossRef]
9. Zarei, S.F.; Mokhtari, H.; Ghasemi, M.A.; Peyghami, S.; Davari, P.; Blaabjerg, F. Control of Grid-Following Inverters under Unbalanced Grid Conditions. *IEEE Trans. Energy Convers.* **2020**, *35*, 184–192. [CrossRef]
10. Zarei, S.F.; Ghasemi, M.A.; Khankalantary, S. Current limiting strategy for grid-connected inverters under asymmetrical short circuit faults. *Int. J. Electr. Power Energy Syst.* **2021**, *131*, 107020. [CrossRef]
11. Zarei, S.F.; Ghasemi, M.A.; Mokhtari, H.; Blaabjerg, F. Performance Improvement of AC-DC Power Converters under Unbalanced Conditions. *Sci. Iran.* **2019**, 3273–3511. [CrossRef]
12. Ghasemi, M.A.; Zarei, S.F.; Peyghami, S.; Blaabjerg, F. A Theoretical Concept of Decoupled Current Control Scheme for Grid-Connected Inverter with L-C-L Filter. *Appl. Sci.* **2021**, *11*, 6256. [CrossRef]
13. Kukkola, J.; Hinkkanen, M.; Zenger, K. Observer-Based State-Space Current Controller for a Grid Converter Equipped with an LCL Filter: Analytical Method for Direct Discrete-Time Design. *IEEE Trans. Ind. Appl.* **2015**, *51*, 4079–4090. [CrossRef]
14. Cheng, C.; Xie, S.; Tu, L.; Tan, L.; Qian, Q.; Xu, J. Single Grid-Current Sensor-Controlled Weak-Grid-Following Inverters: A State-and-Disturbance-Observer-Based Robust Control Scheme Achieving Grid-Synchronization and Disturbance Rejection. *IEEE Trans. Power Electron.* **2022**, *37*, 13743–13754. [CrossRef]
15. Fantino, R.A.; Busada, C.A.; Solsona, J.A. Observer-Based Grid-Voltage Sensorless Synchronization and Control of a VSI-LCL Tied to an Unbalanced Grid. *IEEE Trans. Ind. Electron.* **2019**, *66*, 4972–4981. [CrossRef]
16. Yang, H.; Zhang, Y.; Liang, J.; Gao, J.; Walker, P.D.; Zhang, N. Sliding-Mode Observer Based Voltage-Sensorless Model Predictive Power Control of PWM Rectifier Under Unbalanced Grid Conditions. *IEEE Trans. Ind. Electron.* **2018**, *65*, 5550–5560. [CrossRef]
17. Gholami-Khesht, H.; Monfared, M.; Golestan, S. Low computational burden grid voltage estimation for grid connected voltage source converter-based power applications. *IET Power Electron.* **2015**, *8*, 656–664. [CrossRef]
18. Rahoui, A.; Bechouche, A.; Seddiki, H.; Abdeslam, D.O. Grid Voltages Estimation for Three-Phase PWM Rectifiers Control Without AC Voltage Sensors. *IEEE Trans. Power Electron.* **2018**, *33*, 859–875. [CrossRef]

19. Tao, Y.; Wu, Q.; Wang, L.; Tang, W. Voltage sensorless predictive direct power control of three-phase PWM converters. *IET Power Electron.* **2016**, *9*, 1009–1018. [CrossRef]
20. Xiahou, K.S.; Liu, Y.; Zhang, L.L.; Li, M.S.; Wu, Q.H. Robust Current Sensorless Control of VSC-Based MTDC Transmissions for Integrating Wind Farms. *IEEE J. Emerg. Sel. Top. Power Electron.* **2021**, *9*, 7383–7394. [CrossRef]
21. Xiahou, K.; Lin, X.; Liu, Y.; Wu, Q.H. Robust Rotor-Current Sensorless Control of Doubly Fed Induction Generators. *IEEE Trans. Energy Convers.* **2018**, *33*, 897–899. [CrossRef]
22. Liu, Z.H.; Nie, J.; Wei, H.L.; Chen, L.; Li, X.H.; Zhang, H.Q. A Newly Designed VSC-Based Current Regulator for Sensorless Control of PMSM Considering VSI Nonlinearity. *IEEE J. Emerg. Sel. Top. Power Electron.* **2021**, *9*, 4420–4431. [CrossRef]
23. Yazdani, A.; Iravani, R. *Voltage-Sourced Converters in Power Systems: Modeling, Control, and Applications*; Wiley-IEEE Press: New York, NY, USA, 2010.
24. Luenberger, D. An introduction to observers. *IEEE Trans. Autom. Control.* **1971**, *16*, 596–602. [CrossRef]